CrossMark

ORIGINAL ARTICLE

The 2010 Beni-Ilmane, Algeria, earthquake sequence: statistical analysis, source parameters, and scaling relationships

Issam Abacha · Oualid Boulahia ·
Abdelkarim Yelles-Chaouche · Fethi Semmane ·
Hamoud Beldjoudi · Hichem Bendjama

Abstract Source parameters were estimated for the 18 largest events ($M_D \geq 4$) of the 2010 Beni-Ilmane earthquake sequence (north-central Algeria) using data recorded by permanent broadband seismic stations of the Algeria Digital Seismic Network (ADSN). Displacement spectra of P and S waves were estimated using a Brune seismic source model to compute spectral parameters. Spectra were corrected to account for path effects and near-surface attenuation. The average seismic moments estimated from P and S wave spectra ranged from 5.5×10^{14} to 1.6×10^{17} N m, with a logarithmic mean $M_0(S)/M_0(P)$ ratio of 0.96. Source radii ranged from 735 to 2266 m with an average $r(S)/r(P)$ value of 0.99. Stress drops varied from 0.2 to 11 MPa with an average $\Delta\sigma(S)/\Delta\sigma(P)$ ratio of 1.08. Corner frequencies (f_c) vary from 0.8 to 2.4 Hz, and moment magnitudes (M_w) range from 3.8 to 5.4. Scaling relations of seismic moments, source radii, and stress drops indicate that events with $M_0 \geq 2 \times 10^{16}$ N m have stress drops that are generally constant, while the stress drops of earthquakes with $M_0 < 2 \times 10^{16}$ N m decrease with decreasing seismic moment. The source parameters of the 1960 Melouza (now Beni-Ilmane) moderate earthquake are also estimated from these scaling relationships. Finally, we find low b and γ values in the Gutenberg–Richter and gamma function laws. The seismic sequence is discussed in the context of the active tectonics of the Beni-Ilmane fault system.

1 Introduction

For a period of several months beginning May 14, 2010, a moderate seismic sequence with an M_D 5.2 mainshock ($I_0 =$ VII; Yelles-Chaouche et al. 2013) affected the Beni-Ilmane region of north-central Algeria, exactly in the transition zone between the Bibans and Hodna mountains (Fig. 1a). This sequence was marked by the occurrence of three successive moderate shocks of $5.0 \leq M_D \leq 5.2$ on at least two faults, which produced a significant number of aftershocks concentrated in a window of 18 days. The first main fault is a subvertical left-lateral strike–slip fault trending NNE–SSW, in which two mainshocks occurred. The second fault, oriented E–W, is a high-angle reverse fault (Yelles-Chaouche et al. 2013). Surface fissures evident in the epicentral region and related to gravitational effects were observed and described in detail by Zazoun et al. (2012). It is notable that this sequence was the second destructive historic event in the region; the first was an M 5.6 event in 1960 (Benhallou 1985; Benouar 1994) (Fig. 1b). The moment magnitudes of the three largest events, obtained from near-field waveform modeling, are M_w 5.5, M_w 5.1, and M_w 5.2, respectively (Beldjoudi et al. 2016). Yelles-Chaouche et al. (2013) analyzed a dataset that included the most significant aftershocks in the sequence; 1403 events were located in their study, the main of which had focal mechanisms calculated from first-motion P wave

I. Abacha (✉) · O. Boulahia · A. Yelles-Chaouche ·
F. Semmane · H. Beldjoudi · H. Bendjama
Centre de Recherche en Astronomie Astrophysique et
Géophysique, CRAAG, BP 63, Bouzaréah, Algiers, Algeria
e-mail: abacha.issam@yahoo.fr

🐾 Springer

polarities (Fig. 1b). Beldjoudi et al. (2016), who presented a more detailed model of the fault system and its relationship to seismotectonics, obtained similar focal mechanism solutions to Yelles-Chaouche et al. (2013) using inversion of broadband velocity waveforms of the three main shocks. Nevertheless, Beldjoudi et al. (2016) attributed each of the three main events to its own fault. More recently, Hamdache et al. (2017) conducted a statistical analysis of this earthquake sequence and found b values in agreement with values observed worldwide for successive occurrence of mainshock–aftershock sequences. Abacha et al. (2014) resolved crustal P wave structure in the epicentral region using well-located aftershocks: the low-velocity anomalies in their model correspond to the alignments of the main faults in the region, and their high-velocity anomalies could correspond to rigid blocks of upper crust. Low-velocity anomalies observed in their S wave model of the aftershock area could indicate regions with high fluid content.

The source parameters of an earthquake, such as the source dimensions, seismic moment, and stress drop, can be determined by spectral analysis of its body and surface wave records. Based on theoretical models, such as the rectangular models of Haskell (1964) and Savage (1972), and the circular models of Brune (1970, 1971) and Madariaga (1976), it is possible to calculate the displacement from a fault model and compare theoretical spectra with experimental results. The use of both P and S wave spectra for the determination of seismic source parameters based on the model of Brune (1970) has been widely adopted; examples include Fletcher (1980) and García et al. (1996, 2004)) for small-sized local earthquakes and Hanks and Wyss (1972) for teleseismic events. In Algeria, a recent source parameter study was performed by Semmane et al. (2015) using P wave data from the M_w 4.1 Bordj-Menaïel earthquake.

In the current study, we estimate earthquake source parameters of the 18 largest events ($M_D \geq 4$) of the 2010 Beni-Ilmane seismic sequence, including the three $M_D \geq 5$ shocks, based on P and S wave displacement spectra and the circular seismic source model of Brune (1970, 1971) (Table 1). The earthquake sequence was characterized by two clusters corresponding to unique faults. In this paper, we apply a statistical test to the time intervals between successive earthquakes to better understand the physical correlations between seismic events from the same cluster. Scaling laws relating the

seismic moment M_0 to other source parameters are developed for the Beni-Ilmane region. Finally, the results are used to estimate the source parameters of the 1960 M_s 5.0 Melouza earthquake (Benouar 1994), which occurred in the same area.

2 Data acquisition and processing

To determine the earthquake source parameters, we used 11 broadband stations from the Algerian permanent seismic network (Yelles-Chaouche et al. 2013b), located 25–450 km from the epicentral area. Stations ABZH, ADJF, CBBR, and EADB are equipped with three-component, ultra-broadband Streckeisen STS-2 sensors coupled to Q330 Quanterra digitizers. Stations ATAF, CABS, CKHR, EMHD, OJGS, and EMHD are equipped with three-component Geodevice BBVS-60s broadband seismometers coupled to Geodevice EDAS-24IP digitizers; station CSVB is equipped with a three-component ultra-broadband Geodevice BBVS-120 sensor coupled to a Geodevice EDAS-24IP digitizer (Fig. 1a). Since the stations installed in hard bedrock, the site effects will be minimized.

The source parameters of the three main shocks and 15 largest aftershocks of the 2010 Beni-Ilmane earthquake sequence were estimated from their P and S wave displacement spectra using three-component data and the following processing steps. First, we selected seismic records with high signal-to-noise ratios (SNR > 3) for both P and S waves. Careful analyst examination identified an electronic problem on the E–W channel of the nearest station (ATAF); consequently, data from this channel were not used.

Signals were corrected by removing the mean and linear trend. A 10% cosine taper was then applied to each end of the signal, and signals were subsequently corrected to translate the instrument response to a common curve. The window lengths around the P and S wave arrivals were manually adjusted to minimize contamination from other phases and to maintain the resolution and stability of the spectra: selection windows ranged from 2 to 8 s, depending on the event magnitude and the epicentral distance of the station. Fourier amplitude spectra were calculated and smoothed using an FFT and a Konno–Omachi log scale window (Konno and Ohmachi 1998). The fit between observed and theoretical displacement spectra led to model the remaining frequencies.
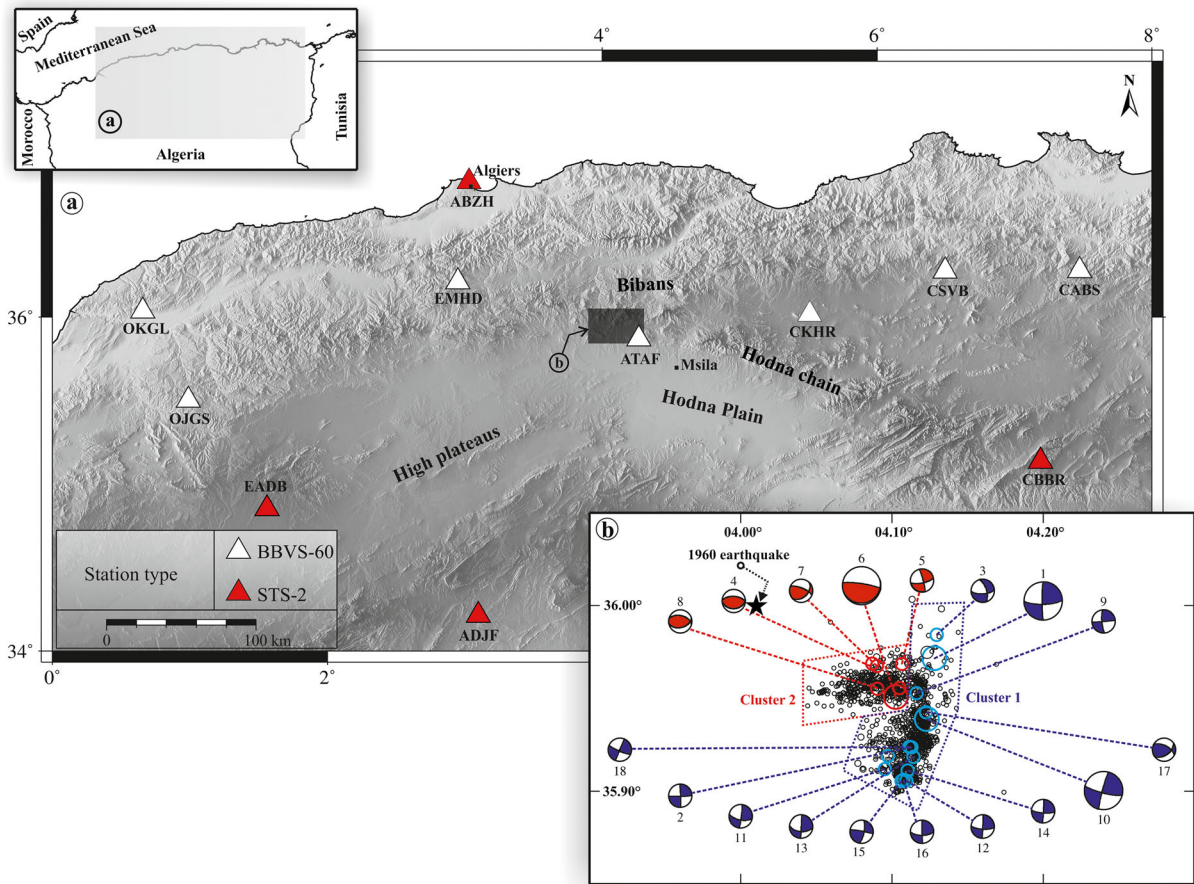
Fig. 1 **a** Map of the study area, including seismic stations used in this work and the main geological units of the region. **b** Horizontal distribution of 1403 relocated events from the first 2 weeks of the sequence, with focal mechanisms of the 18 $M_D \geq 4$ events used in this study. Symbol sizes are proportional to earthquake magnitudes, which were estimated using the formula of Semmane et al. (2012). Events with violet focal mechanisms belong to the first cluster and events with red mechanisms to the second cluster. The black star indicates the 1960 Beni-Ilmane earthquake. The dashed violet rectangle represents the boundary delimited by the first cluster, and the red rectangle represents that delimited by the second. The dark gray box in **a** delineates the geographic boundary of **b**

3 Statistical analysis

Before source parameters were estimated, we performed a statistical analysis to constrain the source process of this seismic sequence. Because earthquakes are not uniformly distributed in time, space, or magnitude, earthquake distributions obey a power law or fractal scaling, often described by the Gutenberg–Richter relationship between magnitude and frequency (Gutenberg and Richter 1944, 1954, 1956) and the modified Omori law that characterizes the decay of aftershock activity (Utsu et al. 1995). Corral (2004), from analysis of a number of seismic catalogs, found that the time intervals of aftershocks are best described by a Gamma distribution. Hainzl et al. (2006) showed that seismic event distributions within a cluster can usually be approximated by a Gamma function, whose parameters are related to the proportion of independent earthquakes

$$\Gamma(\tau) = C\tau^{\gamma-1}e^{-\tau/\beta} \tag{1}$$

where τ is the ratio between the time intervals of successive microseisms Δt ($\Delta t_i = t_i - t_{i-1}$) and the average time interval Δt_0, and C, γ, and β are constants.

The 2010 Beni-Ilmane seismic sequence was characterized by two event clusters (Yelles-Chaouche et al.

Table 1 Fault plane solutions for the 18 largest aftershocks ($M_D \geq 4$). Score and quality are two parameters that measure the similarity between polarities observed and predicted by the model (modified from Yelles-Chaouche et al. 2013)

Number	Date (YY/MM/DD)	Origin time (HH:MM:SS)	MD	Location		Depth (km)	Nodal plane A			Nodal plane B			Score (%)	Quality (%)
				Lon (°E)	Lat (°N)		Strike (°)	Dip (°)	Rake (°)	Strike (°)	Dip (°)	Rake (°)		
1	**10/May/14**	**12:29:20**	**5.2**	**4.13**	**35.97**	**8.2**	**180**	**86**	**15**	**89**	**75**	**173**	**100**	**69**
2	**10/May/14**	**15:13:13**	**4.7**	**4.11**	**35.92**	**6.0**	**88**	**85**	**−177**	**358**	**87**	**−5**	**100**	**63**
3	**10/May/14**	**23:43:22**	**4.4**	**4.13**	**35.98**	**6.9**	**89**	**66**	**−149**	**343**	**61**	**−27**	**100**	**64**
4	10/May/15	00:00:40	4.0	4.09	35.97	9.1	273	58	93	88	32	86	100	73
5	10/May/16	03:51:29	4.8	4.11	35.97	8.3	345	82	−19	78	72	−172	100	71
6	10/May/16	06:52:39	5.0	4.10	35.95	7.4	279	82	94	72	9	64	100	66
7	10/May/16	09:46:01	4.0	4.09	35.97	8.5	292	71	127	45	41	30	100	77
8	10/May/19	23:59:50	4.1	4.09	35.95	7.7	283	49	108	76	44	70	100	71
9	**10/May/21**	**12:16:18**	**4.0**	**4.12**	**35.95**	**7.5**	**85**	**89**	**168**	**176**	**78**	**1**	**100**	**68**
10	**10/May/23**	**13:28:15**	**5.0**	**4.12**	**35.94**	**5.7**	**195**	**85**	**10**	**104**	**80**	**175**	**100**	**67**
11	**10/May/23**	**23:39:54**	**4.1**	**4.09**	**35.91**	**4.7**	**7**	**85**	**−26**	**100**	**64**	**−174**	**100**	**69**
12	**10/May/24**	**21:00:38**	**4.9**	**4.11**	**35.91**	**6.7**	**3**	**88**	**−18**	**93**	**72**	**−178**	**100**	**69**
13	**10/May/24**	**23:48:25**	**4.1**	**4.11**	**35.92**	**6.2**	**3**	**89**	**−35**	**93**	**55**	**−179**	**100**	**75**
14	**10/May/25**	**13:05:09**	**4.5**	**4.11**	**35.91**	**5.3**	**3**	**87**	**−14**	**94**	**76**	**−177**	**100**	**69**
15	**10/May/26**	**17:49:44**	**4.2**	**4.11**	**35.90**	**6.4**	**12**	**73**	**5**	**280**	**85**	**163**	**100**	**67**
16	**10/May/26**	**20:47:39**	**4.3**	**4.11**	**35.91**	**6.4**	**179**	**89**	**25**	**89**	**64**	**179**	**90**	**68**
17	**10/May/30**	**04:48:30**	**4.2**	**4.12**	**35.94**	**5.5**	**55**	**51**	**40**	**297**	**60**	**133**	**100**	**72**
18	**10/May/31**	**16:05:03**	**4.6**	**4.11**	**35.92**	**6.7**	**23**	**89**	**−10**	**113**	**80**	**−179**	**100**	**69**

2013) related to two active faults with activity confined to relatively small geographic regions. To better understand the physical relationship between seismic events in each cluster, we performed a statistical test on the time intervals between successive earthquakes. In Fig. 2, clusters 1 and 2 show a low γ value ($\gamma = 0.46$, i.e., 46% of events are independent); we obtain $\gamma = 0.57$ when both clusters are considered together.

Bernard et al. (2007) suggested two classes of seismic event sequences that can be distinguished by their γ values. If $\gamma < 0.5$, events are correlated and triggering is due to the interaction between events. This class of sequence typically includes a high concentration of aftershocks in time and space. If $\gamma > 0.5$, the events are more independent and triggering is more likely related to forcing mechanisms, such as creep or fluid pressure.

We used the *ZMAP* software package (Wiemer 2001) to calculate the b values of the Gutenberg–Richter law using least-squares and maximum likelihood methods. We obtained b values of $b = 0.85 \pm 0.03$ for cluster 1, $b = 1.03 \pm 0.05$ for cluster 2, and

$b = 0.96 \pm 0.03$ when both clusters were considered together (Fig. 3). Hamdache et al. (2017) obtained $b = 0.96 \pm 0.03$ for their first cluster (which mainly corresponds to cluster 2 of this paper), $b = 1.04 \pm 0.05$ for their second cluster (which mainly corresponds to cluster 1 in this paper), and $b = 0.96 \pm 0.03$ for the entire sequence. The differences between the results of these two studies are related to how the clusters are defined: we considered the first mainshock with a strike–slip solution to be part of a cluster of events dominated by strike–slip motion, whereas Hamdache et al. (2017) considered this event a member of a cluster dominated by reverse faulting. Typical b values of tectonic earthquake sequences are $0.78 \leq b \leq 0.9$ (Gutenberg and Richter 1949, 1954). This suggests that the region is relatively homogeneous, and the effective normal stress is sufficiently high to trigger moderate to strong earthquakes.

From these two statistical laws, we note that this seismic sequence is likely related to the active tectonics of the Beni-Ilmane fault system and was triggered by interactions among seismic events.
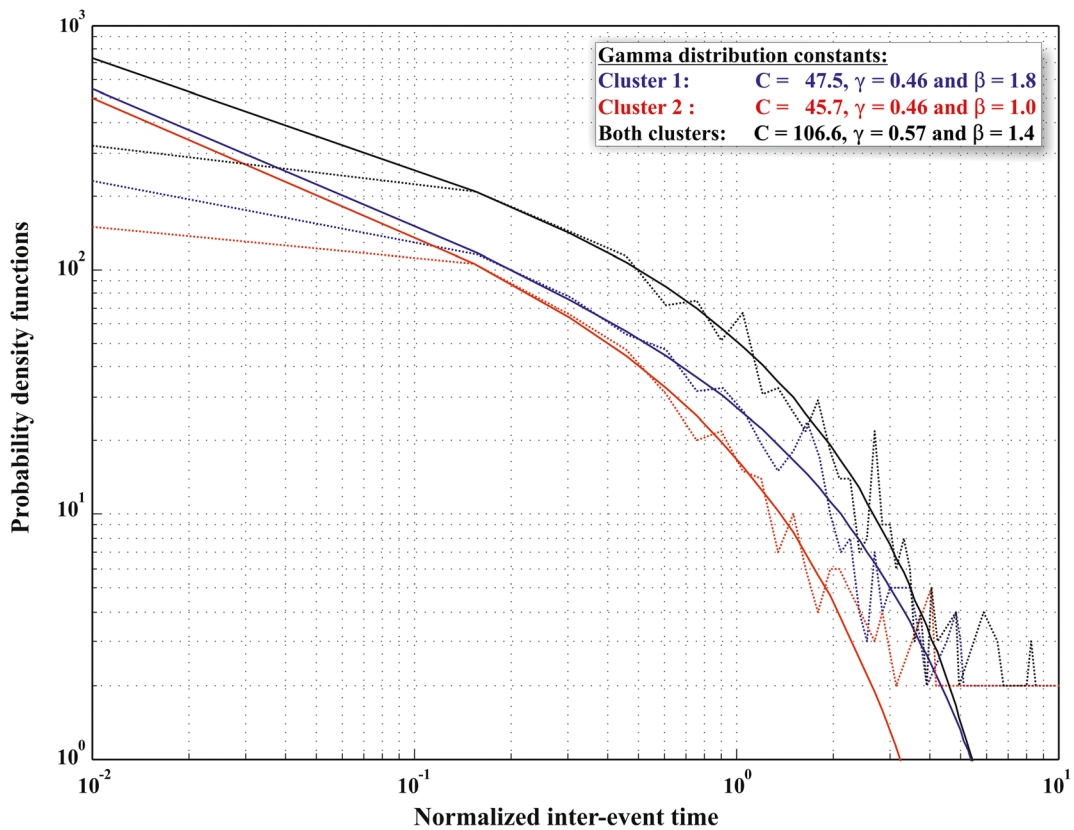
Fig. 2 Probability density functions of normalized inter-event times for cluster 1 (dashed violet line), cluster 2 (dashed red line), and both clusters (dashed black line). The best-fit gamma distributions are indicated by the corresponding solid lines of each color

4 Source parameter estimation

4.1 Methodology

The methodology used to determine source parameters from P and S wave spectra is commonly used and has been described in several previous works, including detailed discussions by Hanks and Wyss (1972), Fletcher (1980), and García et al. (1996, 2004)). We estimate earthquake source parameters based on a circular seismic source model (Brune 1970, 1971). The displacement amplitude spectra of a P or S wave at frequency f can be described by the relationship

$$A_d(f) = \frac{G(\Delta, h)D(f)M_0 FR_{(\theta, \phi)}}{4\pi\rho V^3 \left(1 + \dfrac{f^2}{f_c^2}\right)} \qquad (2)$$

where Δ is the epicentral distance, h is the hypocentral depth, $G(\Delta, h)$ is the geometrical spreading term (in this case, $G = 1/\Delta$), f is the frequency, f_c is the corner

frequency, ρ is density, V is the phase velocity (P or S) at the source, M_0 is seismic moment, and $FR_{(\theta, \phi)}$ is a factor to correct for the free surface effect and radiation pattern, respectively. The diminution function $D(f)$ in Eq. (2) is representative of the attenuation path and can be written as

$$D(f) = P(f)e^{\frac{-\pi f t}{Q}} \qquad (3)$$

The anelastic attenuation term $e^{\frac{-\pi f t}{Q}}$ and the term that describes the attenuation of seismic waves near the site $P(f)$, which is equal to $e^{-\pi k f}$, are both frequency-dependent (Singh et al. 1982). According to Anderson and Hough (1984), the factor k is used to parameterize the slope of the high-frequency band; in this study, a k value of ~ 0.02 s has been considered as the most used average value (Singh et al. 1982; García et al. 2004). The parameter t in Eq. (3) represents the elapsed time from the earthquake origin time to the beginning of the spectral window; when the latter coincides with the arrival times, $t = 1.33\Delta t_{sp}$ for P waves and $t = \Delta t_{sp} + 1.33\Delta t_{sp}$ for S waves, assuming $V_P/V_S = 1.75$ (Yelles-

Fig. 3 Frequency–magnitude distributions of cluster 1 (violet), cluster 2 (red), and both clusters combined (black). Circles denote the cumulative number of events as a function of magnitude. Curves correspond to number of events vs. magnitude. Straight lines give the best-fit linear relationships
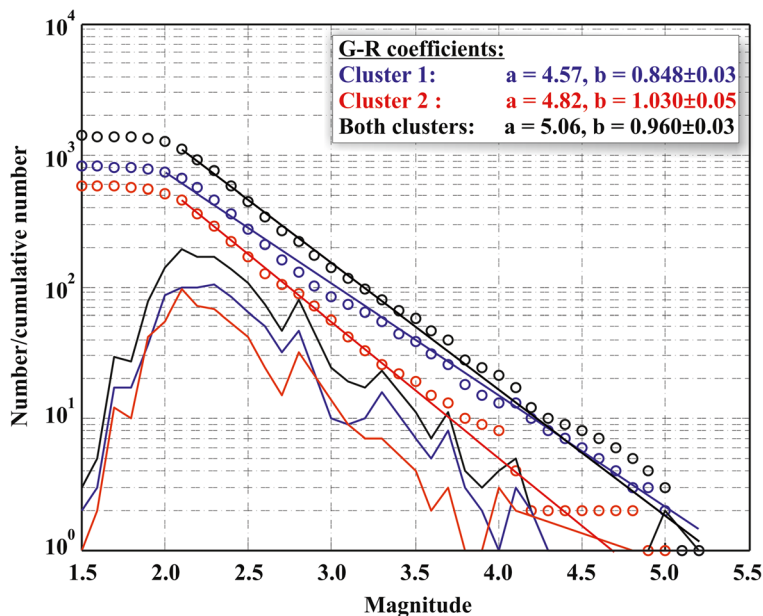
Chaouche et al. 2013); the term Δt_{sp} is shorthand for the difference between the arrival times of the S and P waves. In Eq. (3), Q is the quality factor, which potentially depends on frequency, $Q = q_0 f^{q_\alpha}$, where q_0 is a spectral amplitude correction (here, $q_0 = 500$ for P waves and 250 for S waves); typically, $q_\alpha \cong 0.7$ (Beldjoudi et al. 2016).

The following equations were used to calculate the seismic moment M_0, the source radius r, the stress drop $\Delta\sigma$, and the average displacement U, respectively:

$$M_0 = \frac{4\pi\rho V^3 \Delta\Omega_0}{FR_{(\theta,\phi)}} \qquad (4)$$

$$r = \frac{2.34}{2\pi} \frac{V}{f_c} \qquad (5)$$

$$\Delta\sigma = \frac{7}{16} \frac{M_0}{r^3} \qquad (6)$$

$$U = \frac{M_0}{\mu\pi r^2} \qquad (7)$$

where ρ is density (here, 2700 kg/m³); V is the phase velocity near the source (here, $V_P = 5.2$ km/s and $V_S = 3$ km/s, adapted from the velocity model of Yelles-

Chaouche et al. 2013); Δ is the hypocentral distance; Ω_0 is the low-frequency level; μ is shear modulus (here, assumed to be 3×10^{10} N/m²); f_c is the corner frequency; and $R_{(\Theta, \Phi)}$ is the radiation pattern coefficient. In the present study, $R_{(\Theta, \Phi)} = 0.52$ for P and 0.63 for S (Boore and Boatwright 1984). The factor F was included in Eq. (4) to account for wave amplification at the free surface. An average value of 1.0 was estimated for the F coefficient (Aki and Richards 1980) based on the incidence angles observed. However, small changes in F do not significantly alter the calculated values of the seismic moment and energy. The moment magnitude can be calculated from the above equations using the formula of Hanks and Kanamori (1977),

$$M_w = (2/3)\log M_0 - 6.0 \qquad (8)$$

where M_0 is in Newton meters.

4.2 Results

To determine the source parameters of the 18 largest events of the 2010 Beni-Ilmane earthquake sequence, a MATLAB program was developed to automatically estimate spectral parameters: the low-frequency displacement spectral level Ω_0 and corner frequency f_c are based on fitting the displacement spectrum in Eq. (2) to the observed spectrum. We obtain the best value of f_c based L1 norm inversion. Displacement spectra (e.g., Fig. 4)
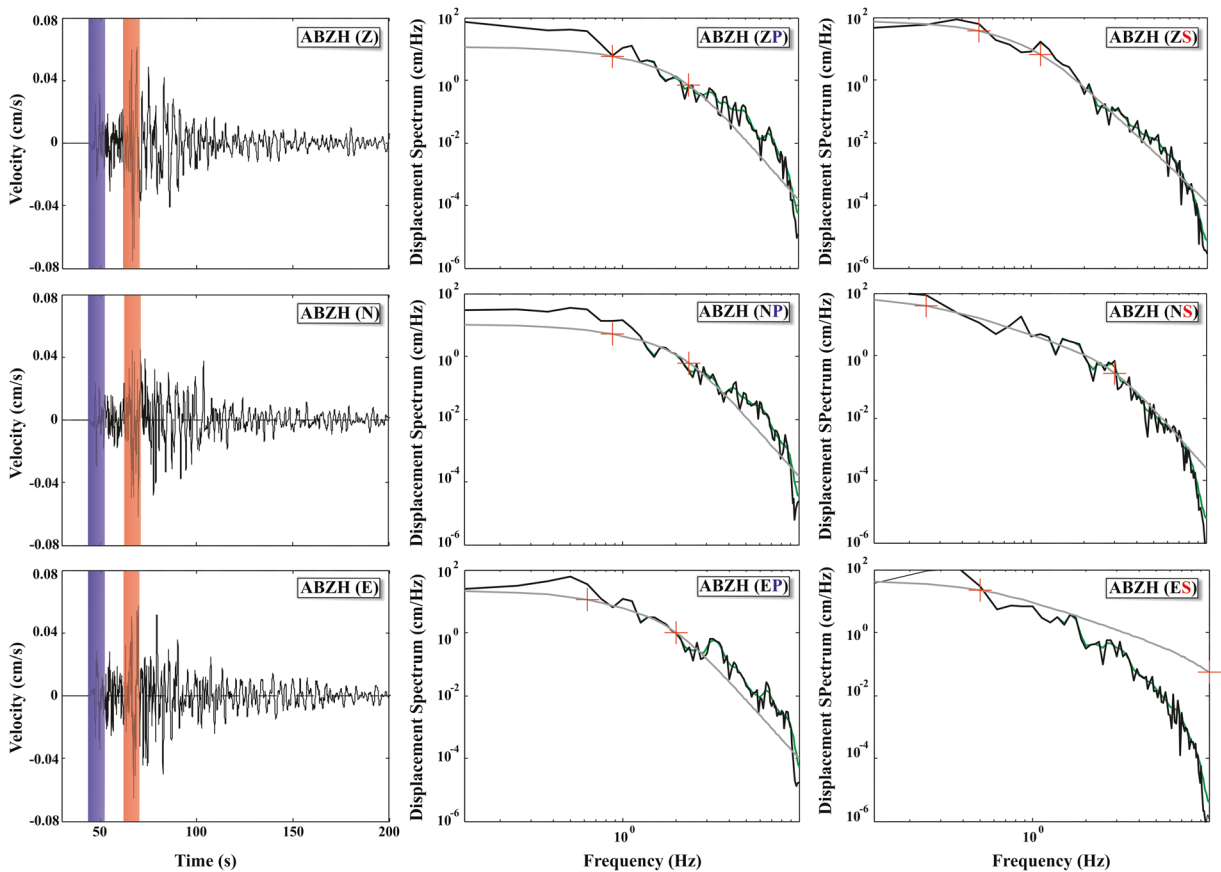
Fig. 4 Sample displacement spectra of an event recorded at station ABZH. Left panel: instrumentally corrected three-component velocity seismograms from the 14 May 2010 mainshock (M_D 5.2). Violet- and red-shaded areas indicate the time windows used for P and S wave trains, respectively. Middle and right panels: Displacement spectra of the seismograms shown (P waves, middle panel; S waves, right panel). Gray lines are fitted spectra. Red crosses represent low-frequency plateaus Ω_0 with corner frequencies f_c and with f_{max}

were corrected for attenuation and smoothed by applying a Konno–Omachi log scale window and finally fitted by theoretical spectra. It is important to note that some components show a poor fit between theoretical and experimental spectra (for example subplot down on the right in Fig. 4); for this reason, these components were excluded.

The low-frequency displacement spectral level of the total spectrum is equal to the square root of the sum of the squared values of each component at flat levels. The value of the corner frequency was averaged over the three components of each station. Calculations of source parameters were made using P and S wave data from 774 spectra for the 18 events, separately as well as combined. The average values of each parameter x (M_0 (P, S) and f_c (P, S)) are estimated using the following formulae (Archuleta et al. 1982):

$$\langle x \rangle = \text{antilog} \left\{ \frac{1}{\text{NS}} \sum_{i=1}^{\text{NS}} \log x_i \right\} \qquad (9)$$

$$\text{s.d.}(\log \langle x \rangle) = \left\{ \frac{1}{\text{NS}-1} \sum_{i=1}^{\text{NS}} [\log x_i - \log \langle x \rangle]^2 \right\}^{1/2} \qquad (10)$$

$$\text{E}\langle x \rangle = \text{antilog} \{ \text{s.d.}(\log \langle x \rangle) \} \qquad (11)$$

where x denotes the average value of 𝕩, NS is the number of the stations used, *s.d.* is the standard deviation, and E⟨x⟩ is the multiplicative error factor for 𝕩.

The source radius at each station using Brune's model was given by the Eq. (5), and the average source radius r was computed:

Table 2 Average values (from *P* and *S* waves) of f_c, M_0, r, and $\Delta\sigma$ with multiplicative error factors EM_0 and Ef_c, and the mean values of M_w and U. f_c is the corner frequency in Hertz; M_0 is the average seismic moment in Newton meter; r is the average source radius in meters; $\Delta\sigma$ is the average stress drop in megapascals; U is the average displacement in meters. Events with bold values belong to the first cluster; events with italicized values belong to the second cluster

Number	$<f_c>$	Ef_c	$<M_0>$	EM_0	$<M_w>$	$<r>$	$<\Delta\sigma>$	$<U>$
1	**0.8**	**1.18**	**1.6e+17**	**1.25**	**5.4**	**2266**	**5.8**	**0.32**
2	**1.5**	**1.23**	**4.6e+16**	**3.65**	**5.0**	**1220**	**11.0**	**0.33**
3	**1.4**	**1.14**	**7.0e+15**	**2.31**	**4.5**	**1207**	**1.7**	**0.05**
4	*2.2*	*1.22*	*1.2e+15*	*1.87*	*4.0*	*735*	*1.3*	*0.02*
5	*1.3*	*1.16*	*1.0e+16*	*1.72*	*4.6*	*1380*	*1.7*	*0.06*
6	*0.9*	*1.21*	*1.1e+17*	*1.69*	*5.3*	*1879*	*7.0*	*0.32*
7	*1.8*	*1.25*	*1.5e+15*	*1.86*	*4.1*	*1070*	*0.5*	*0.01*
8	*1.7*	*1.25*	*5.5e+14*	*1.93*	*3.8*	*980*	*0.2*	*0.01*
9	*2.4*	*1.36*	*9.5e+14*	*1.78*	*3.9*	*797*	*0.8*	*0.02*
10	**1.0**	**1.17**	**7.1e+16**	**1.42**	**5.2**	**1737**	**5.9**	**0.25**
11	**1.6**	**1.25**	**4.4e+15**	**3.09**	**4.4**	**1129**	**1.3**	**0.04**
12	**1.3**	**1.20**	**9.1e+15**	**1.51**	**4.6**	**1517**	**1.1**	**0.04**
13	**2.2**	**1.36**	**9.8e+14**	**1.40**	**3.9**	**1068**	**0.3**	**0.01**
14	**1.5**	**1.22**	**1.0e+16**	**1.97**	**4.6**	**1258**	**2.2**	**0.07**
15	**1.5**	**1.23**	**1.5e+16**	**2.03**	**4.7**	**1230**	**3.5**	**0.10**
16	**1.5**	**1.22**	**6.4e+15**	**2.05**	**4.5**	**1272**	**1.4**	**0.04**
17	**1.8**	**1.44**	**2.8e+15**	**2.07**	**4.2**	**1200**	**0.7**	**0.02**
18	**1.6**	**1.24**	**5.6e+15**	**1.49**	**4.4**	**1202**	**1.4**	**0.04**

$$r = \frac{1}{NS} \sum_{i=1}^{NS} r_i \qquad (12)$$

where r_i is the radius determined from the corner frequency at the *i*th station. The mean stress drop $\Delta\sigma$ was calculated using the mean moment and mean radius in equation 6.

Table 2 presents the average values (obtained from *P* and *S* data) of f_c, M_0, r, and $\Delta\sigma$ and with multiplicative error factors EM_0 and Ef_c, in addition to calculated mean values of M_w and U. Given the linear relation linked f_c to r the estimated error factor will be the same. Seismic moment values M_0 range from 5.5×10^{14} to 1.6×10^{17} N m, source radii range from 735 to 2266 m, stress drops range from 0.2 to 11 MPa, corner frequencies (f_c) from 0.8 to 2.4 Hz, and moment magnitudes (M_w) from 3.6 to 5.4. The seismic moments and moment magnitudes of the three largest shocks are comparable to the results of Beldjoudi et al. (2016) and the estimates produced by various seismological centers: ETHZ (Swiss Federal Institute of Technology, Zurich, Switzerland), GCMT (Global Centroid Moment Tensor, USA),

INGV (Istituto Nazionale di Geofisica e Vulcanologia, Italy), and IGN (Instituto Geográfico Nacional, Spain).

In Fig. 5a, we show the values of corner frequencies obtained from *S* wave windows vs. the values obtained from *P* wave windows. *P* wave corner frequencies higher than the *S* wave corner frequencies are frequently observed (e.g., Molnar et al. 1973; Fletcher 1980; Tusa and Gresta 2008; Ataeva et al. 2014); therefore, circular source models such as that proposed by Brune (1970) are more suitable for this study than rectangular models such as those of Haskell (1964) and Savage (1972), which expect approximately equal corner frequencies for *P* and *S* waves, making them ill-suited to descriptions of moderate and small earthquakes (Modiano 1980). Consistent with the claim of Hanks and Wyss (1972) that $f_c(P)$ should be shifted relative to $f_c(S)$ by a factor of V_P/V_S, our results yield an average ratio of $f_c(P)/f_c(S) = 1.70$.

To check our evaluation of the low-frequency level Ω_0 and the corner frequency f_c, we show $M_0(S)$ vs. $M_0(P)$, $r(S)$ vs. $r(P)$, and $\Delta\sigma(S)$ vs. $\Delta\sigma(P)$ in Fig. 5b–d. The low-frequency asymptote is directly related to seismic moment by Eq. (4), and the corner frequency is
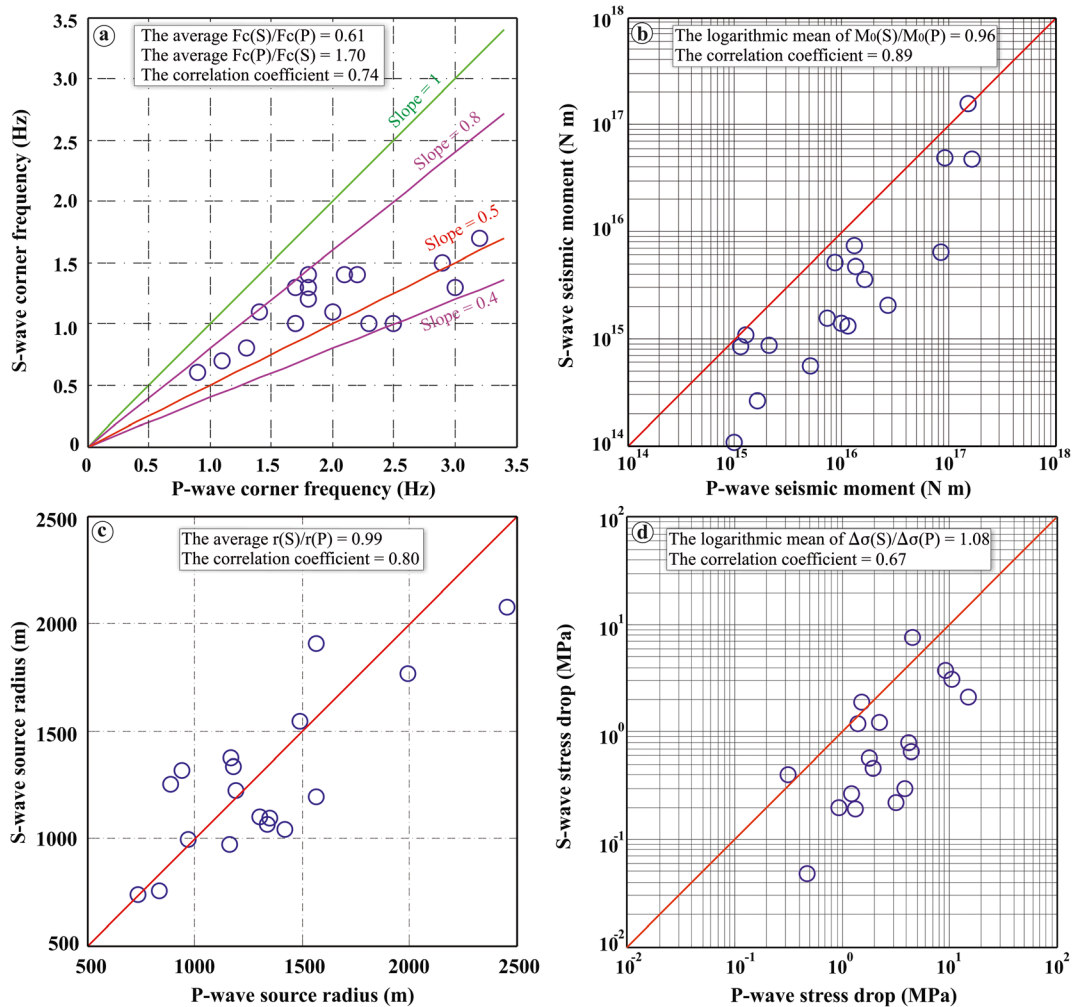
Fig. 5 Comparisons between source parameters f_c, M_0, r, and $\Delta\sigma$ obtained from P and S waves. **a** S wave corner frequencies $f_c(S)$ vs. P wave corner frequencies $f_c(P)$ with constant slopes indicated by straight lines. **b** Correlation between S wave and P wave seismic moments. The red straight line represents $M_0(P) = M_0(S)$. **c** Correlation between S and P wave source radii, r. The straight line represents $r(P) = r(S)$. **d** S wave stress drop vs. P wave stress drop. The straight line represents $\Delta\sigma(P) = \Delta\sigma(S)$

inversely related to the source radius by Eq. (5). The logarithmic mean of $M_0(S)/M_0(P)$ is 0.96, and the correlation coefficient between the two is 0.89, which suggests that the radiation pattern correction was adequate and the technique for evaluating the low-frequency level on the seismic spectrum was correctly applied. The average source radius ratio $r(S)/r(P) = 0.99$ and the two variables yield a correlation coefficient of 0.80, indicating consistent evaluation of the corner frequency and empirical validation of the relation indicated by Hanks and Wyss (1972). The results of this checkup have also allowed us to merge the estimations from P and S waves. Indeed, the logarithmic mean ratio between stress drops computed from S and P waves is

1.08 and the two quantities yield a correlation coefficient of 0.67, showing acceptable agreement between the $\Delta\sigma(P)$ and $\Delta\sigma(S)$ estimates.

5 Scaling laws

Scaling laws define the relationships between different pairs of earthquake source parameters. Empirical formulae are typically used to relate seismic moments to duration magnitudes, source radii, and stress drops. The relation between average log M_0 from P and S waves and M_D is plotted in Fig. 6a. The best-fit line to the data in a least-squares sense is
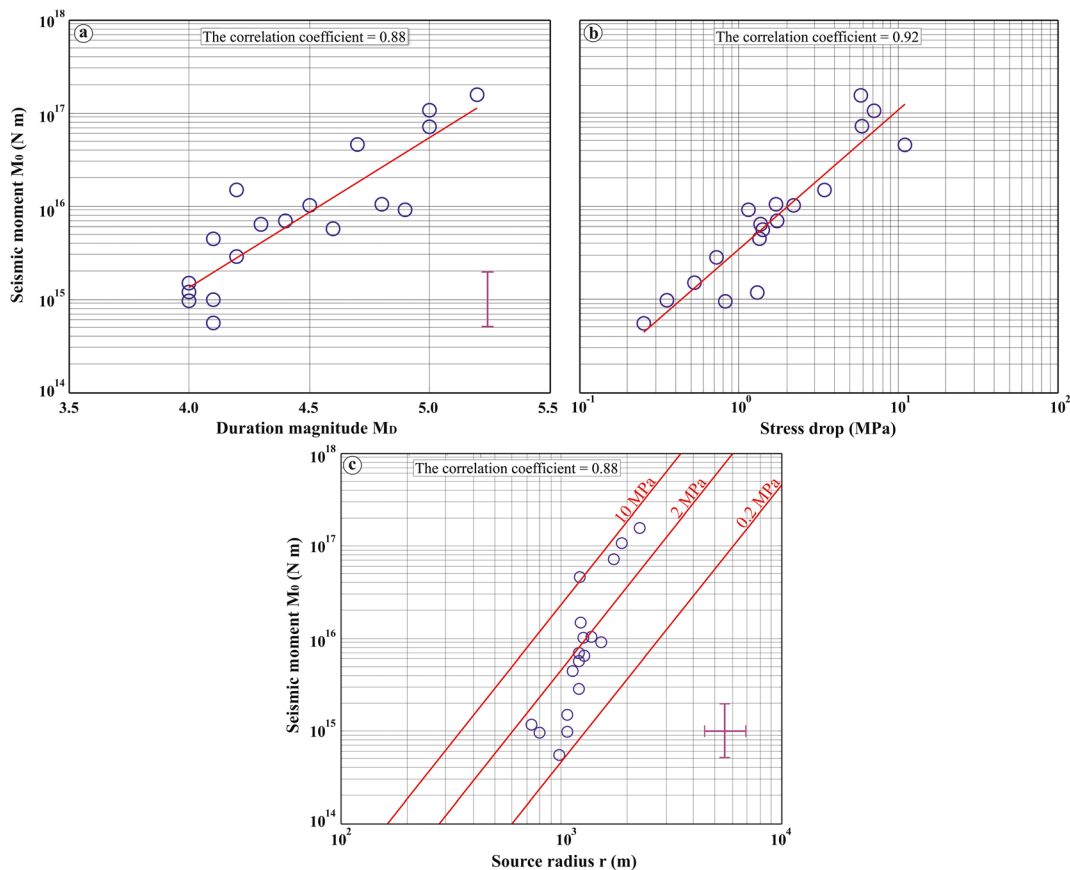
Fig. 6 Relationships between seismic moment M_0 and **a** duration magnitude M_D, **b** stress drop $\Delta\sigma$, and **c** source radius r, calculated from P and S waves. The straight lines in **a** and **b** are the least-squares best-fit lines to the data with average error bar for M_0. Lines of constant stress drop are shown as straight red lines and the averaged error bars are represented in **c**

$$\log M_0(P, S) = (1.60 \pm 0.11)M_D + (8.71 \pm 0.04)$$ with a correlation coefficient of 0.88 between M_0 and M_D. The relation between $\log M_0$ and stress drop $\Delta\sigma$ is shown in Fig. 6b. Applying a linear least-square fit to the data gives the relationship

$$\log M_0(P, S) = (1.50 \pm 0.12)\log\Delta\sigma + (15.53 \pm 0.05)$$ while the correlation coefficient of 0.92 between M_0 and $\Delta\sigma$ indicates that the data points show a high degree of linear correlation. However, a trend of decreasing stress drop with decreasing seismic moment is clearly observed; the three main shocks ($M_w > 5$) are exceptions, with roughly constant stress drop values of ~ 6 MPa.

In Fig. 6c, $\log M_0$ is plotted as a function of $\log r$, the source radius, and lines of constant stress drop are shown. These lines, each of which has a slope of 3.0, are determined from Eq. (6); hence, it follows that $M_0 \propto r^3$. The observed trend is an increase in fault radius with increasing seismic moment. The relation obtained for M_0 as a function of r is

$$\log M_0(P, S) = (5.35 \pm 0.35)\log r - (0.69 \pm 0.04)$$

The correlation coefficient of 0.88 indicates a good correlation between these events. The average value of EM_0 was 1.95; the average value of Ef_c was 1.24. These average values are shown as error bars. The average error associated to stress drop should be within our measurements which does not go beyond 1.95.

The general slope of the regression line in Fig. 6c is $m = 5.3$, i.e., greater than the expected value of 3.0. Detailed examination suggests $m \cong 3$ for events with seismic moments greater than $\sim 2 \times 10^{16}$ N m ($M_w > 5$), with much greater slope for earthquakes with seismic moment less than $\sim 2 \times 10^{16}$ N m. Many previous authors have found similar results (e.g., Archuleta et al. 1982; Centamore et al. 1997). Thus, events with seismic moments greater than $\sim 2 \times 10^{16}$ N m have stress drops that are generally constant, around 6 MPa, while earthquakes with $M_0 < \sim 2 \times 10^{16}$ N m have stress drops that decrease with decreasing moment.

In the context of Aki ([1967]), a breakdown in self-similarity is seen in events with $M_0 > 2 \times 10^{16}$ N m; at lower seismic moments, the stress drop increases with increasing seismic moment. This breakdown could be explained at low magnitudes by a number of factors, including site effects (e.g., Hanks [1982]), attenuation (e.g., Fletcher et al. [1986]), or source effects (e.g., Aki [1984]).

We applied these scaling laws to determine the source parameters of the 21 February 1960 Melouza (now Beni-Ilmane) earthquake (Benouar [1994]). This event is of particular interest because its epicenter was close to the 2010 Beni-Ilmane event, and its macroseismic epicenter is close to Beni-Ilmane. The 1960 event had a CRAAG catalog magnitude of M_D 5.6 and an estimated M_s 5.0 (Benouar [1994]). The maximum intensity was VIII (MSK); the earthquake resulted in 47 deaths, 129 injuries, and about 600 destroyed houses, which left 4900 homeless. Benouar ([1994]) did not attempt to determine the causative fault. Given $M_D = 5.6$, we obtained a seismic moment $M_0 = 5 \times 10^{17}$ N m, a moment magnitude $M_w = 5.8$, a source radius $r = 2.7$ km, and a stress drop $\Delta\sigma = 10.5$ MPa. The value seems too high given the resulted intensity VIII; we suspect an overestimate of the magnitude M_D. To verify this hypothesis, using the magnitude $M_s = 5$ (Benouar [1994]), we applied a relationship for the conversion of M_s to log (M_0) which is suitable for the European area provided by (Ambraseys and Free [1997]); we got a value of the moment $M_0 = 1.25 \times 10^{17}$ N m which gives by applying our law of scale a values of $M_D = 5.2$ and $\Delta\sigma = 5.8$ MPa.

From the results and scaling relations obtained by this study, we can check whether stress transfer occurred between the 1960 and 2010 events. The use of source parameters and scaling laws to calculate empirical GMPEs is of foremost importance because the assessment of earthquake hazard to engineered structures requires ground motion relations that accurately characterize peak ground motions and response spectra as functions of earthquake magnitude and distance. These topics will be the subject of future work.

6 Conclusions

We examined 774 spectra from both P and S waves of the 18 largest events ($M_D \geq 4$) of the 2010 Beni-Ilmane seismic sequence, recorded by 11 three-component broadband seismic stations. Estimated average corner frequencies range from 0.8 to 2.5 Hz with $f_c(P) > f_c(S)$, similar to the results reported by many other authors. Seismic moments M_0 range from 5.5×10^{14} to 1.6×10^{17} N m, source radii r from 735 to 2266 m, and stress drops $\Delta\sigma$ from 0.2 to 11 MPa. The average value of log $M_0(S)$/log $M_0(P) = 0.96$, the average $r(S)/r(P) = 0.99$, and the average log $\Delta\sigma(S)$/log $\Delta\sigma(P) = 1.08$. These results suggest that the technique for evaluating the low-frequency levels and corner frequencies of seismic spectra was correctly applied, and they empirically validate the relationships presented by Hanks and Wyss ([1972]).

Our empirical scaling relations show strong linear correlations and indicate that events with moments $M_0 > 2 \times 10^{16}$ N m have stress drops that are generally constant, while smaller earthquakes have stress drops that decrease with decreasing M_0. The source parameters of the 1960 Melouza (now Beni-Ilmane) earthquake, deduced from these scaling relationships, suggest a seismic moment $M_0 = 5 \times 10^{17}$ N m (M_w 5.8), a source radius $r = 2.7$ km, and a stress drop $\Delta\sigma = 10.5$ MPa. From these results, we can check whether stress transfer occurred between the 1960 and 2010 events. These results could also be used for estimates of strong ground motion.

Finally, the Gutenberg–Richter relationship showed a low b value ($b \leq 1$) and the gamma function also showed a low γ value ($\gamma \leq 0.5$). From these two statistical laws, we conclude that these earthquakes are from a typical tectonic sequence triggered by the interactions between several seismic events. Also, these results suggest that the region is relatively homogeneous, with high values of effective normal stress, suitable for triggering moderate to strong earthquakes.

This study is of importance because the empirical relationships between seismic moment and other earthquake source parameters could improve our understanding of other seismic sequences in northeastern Algeria. For example, the 2012–2013 Bejaia seismic sequence and the 2017 seismic sequence along the North Constantine Fault remain to be studied using these techniques.

References

Abacha I, Koulakov I, Semmane F, Yelles-Chaouche A (2014) Seismic tomography of the area of the 2010 Beni-Ilmane earthquake sequence, north central Algeria. Springer Plus https://doi.org/10.1186/2193-1801-3-650, 3, 650

Aki K (1967) Scaling law of seismic spectrum. J Geophys Res 72:1217–1231

Aki K and Richards PG (1980) Quantitative seismology: theory and methods, vols. 1 and 2. Freeman, San Francisco, CA

Aki K (1984) Asperities, barriers, characteristic earthquakes and strong motion prediction. J Geophys Res 89(B7):5867–5872

Ambraseys NN, Free MW (1997) Surface wave magnitude calibration for European region earthquakes. J Earthq Eng 1(1):1–22

Anderson JG, Hough SE (1984) A model for the shape of the Fourier amplitude spectrum of acceleration at high frequencies. Bull Seismol Soc Am 74:1969–1993

Archuleta RJ, Cranswick E, Mueller C, Spudich P (1982) Source parameters of the 1980 Mammoth Lakes, California, earthquake sequence. J Geophys Res 87:4595–4697

Ataeva G, Shapira A, Hofstetter A (2014) Determination of source parameters for local and regional earthquakes in Israel. J Seismol ISSN 1383-4649 J Seismol. doi https://doi.org/10.1007/s10950-014-9472-x

Beldjoudi H, Delouis B, Djellit H, Yelles-Chaouche A, Gharbi S, Abacha I (2016) The Beni-Ilmane (Algeria) seismic sequence of May 2010: seismic sources and stress tensor calculations. Tectonophysics 670:101–114. https://doi.org/10.1016/j.tecto.2015.12.021

Benhallou H (1985) Les catastrophes sismiques de la région d'Echelif dans le contexte de la sismicité historique de l'Algérie, Thèse de Doctorat. USTHB. Alger 294

Benouar D (1994) Materials for the investigation of the seismicity of Algeria and adjacent regions during the twentieth century. Ann Geofis 37(4):459–860.

Bernard P, Boudin F, Bourouis S, Patau G (2007) Transitoires de déformation dans le Rift de Corinthe. Communication orale, 3F Workshop, Nancy, France

Boore DM, Boatwright J (1984) Average body-wave radiation coefficients. Bull Seismol Soc Am 74:1615–1621

Brune JN (1970) Tectonic stress and the spectra of seismic shear waves from earthquakes. J Geophys Res 75:4997–5009

Brune JN (1971) Correction (to Brune 1970). J Geophys Res 76:5002

Centamore C, Montalto A, Patanè G (1997) Self-similarity and scaling relations for microearthquakes at Mt. Etna volcano (Italy). Phys Earth Planet Inter 103:165–177. https://doi.org/10.1016/S00319201(97)00030-7

Corral A (2004) Long-term clustering, scaling, and universality in the temporal occurrence of earthquakes. Phys Rev Lett 92:108501

Fletcher JB (1980) Spectra from high-dynamic range digital recordings of the Oroville, California aftershocks and their source parameters. Bull Seismol Soc Am 70:735–755

Fletcher JB, Haar LC, Vernon FL, Brune JN, Hanks TC, Berger J (1986) The effects of attenuation on the scaling of source parameters for earthquakes at Anza, California. In: Das, J., Boatwright, J., Scholtz, C.H. (Eds.), Earthquake source mechanics, Geophys. Monogr. Am. Geophys. Union, 57, pp. 331–338

García JM, Vidal F, Romacho MD, Martín-Marfil JM, Posadas A, Luzón F (1996) Seismic source parameters for microearthquakes and small earthquakes of the Granada basin (Southern Spain). Tectonophysics 261:51–66

García JM, Romacho MD, Jiménez A (2004) Determination of near-surface attenuation, with κ parameter, to obtain the seismic moment, stress drop, source dimension and seismic energy for microearthquakes in the Granada Basin (Southern Spain). Phys Earth Planet Inter 141:9–26

Gutenberg B, Richter C (1944) Frequency of earthquakes in California. Bull Seismol Soc Am 34:185–188

Gutenberg B, Richter C (1949) Seismicity of the Earth and associated phenomena. Princeton University Press

Gutenberg B, Richter Ch (1954) Seismicity of the Earth and associated phenomena 2nd Edn: Princeton University Press

Gutenberg B, Richter C (1956) Earthquake magnitude, intensity, energy and acceleration. Bull Seismol Soc Am 46:105–145

Hamdache M, Pelaez JA, Gospodinov D, Henares J (2017) Statistical features of the 2010 Beni-Ilmane, Algeria, aftershock sequence. Pure Appl Geophys 175:773–792. https://doi.org/10.1007/s00024-017-1708-6

Hanks T, Wyss M (1972) The use of body wave spectra in the determination of seismic parameters. Bull Seismol Soc Am 62:561–589

Hanks TC, Kanamori H (1977) A moment magnitude scale. J Geophys Res 84:2348–2350

Hanks TC (1982) fmax. Bull Seismol Soc Am 72:1867–1879

Hainzl S, Scherbaum F, Beauval C (2006) Estimating background activity based on interevent-time distribution. Bull Seismol Soc Am 96(1):313–320. https://doi.org/10.1785/0120050053

Haskell N (1964) Total energy and energy spectral density of elastic wave radiation from propagating faults. Bull Seismol Soc Am 54:1811–1841

Konno K, Ohmachi T (1998)Ground-motion characteristics estimated from spectral ratio between horizontal and vertical components of microtremor. Bull Seismol Soc Am 88:228–241

Madariaga R (1976) Dynamics of an expanding circular fault. Bull Seismol Soc Am 66:639–666

Modiano T (1980) Géophysique et Sismotectonique des Pyrénées occidentales -Etude détaillée du contenu spectral des ondes de volume dans la région focale-. Thèse de doctorat 3 cycle en Géophysique, Grenoble, Institut de Recherches Interdisciplinaires de Geologie et de Mecanique, 188 p

Molnar P, Tucker B, Brune JB (1973) Corner frequencies of P and S waves and models of earthquake source. Bull Seismol Soc Am 63:2091–2104

Savage JC (1972) Relation of corner frequency to fault dimensions. J Geophs Res 77:3788–3795

Semmane F, Abacha I, Yelles-Chaouche AK, Haned A, Beldjoudi H, Amrani A (2012) The earthquake swarm of December 2007 in the Mila region of northeastern Algeria. Nat Hazards 64:1855–1871. https://doi.org/10.1007/s11069-012-0338-7

Semmane F, Benabdeloud BYN, Beldjoudi H, Yelles-Chaouche A (2015) The 22 February 2014 Mw 4.1 Bordj-Menaïel earthquake, near Boumerdes-Zemmouri, North-Central Algeria. Seismol Res Lett 86(3):794–802. https://doi.org/10.1785/0220140196

Singh SK, Apsel RJ, Fried J, Brune JN (1982) Spectral attenuation of SH waves along the Imperial fault. Bull Seismol Soc Am 72(6):2003–2016

Tusa G, Gresta S (2008) Frequency-dependent attenuation of Pwaves and estimation of earthquake source parameters in southeastern Sicily, Italy. Bull Seismol Soc Am 98:2772–2794

Utsu T, Ogata Y, Matsu'ura RS (1995) The centenary of the Omori formula for a decay law of aftershock activity. J Phys Earth 43:1–33

Wiemer S (2001) A software package to analyze seismicity: ZMAP. Seismol Res Lett 72(3):373–382

Yelles-Chaouche AK, Abacha I, Semmane F, Beldjoudi H (2013) The Beni-Ilmane (North Central Algeria) earthquake sequence of May 2010. Pure Appl Geophys https://doi.org/10.1007/s00024-013-0709-3

Yelles-Chaouche AK, Allili T, Alili A, Messemen W, Beldjoudi H, Semmane F, Kherroubi A, Djellit H, Larbes Y, Haned S, Deramchi A, Amrani A, Chouiref A, Chaoui F, Khellaf K, Nait Sidi Said C (2013b) The new Algerian Digital Seismic Network (ADSN): towards an earthquake early-warning system. Adv Geosci 36:31–38. https://doi.org/10.5194/adgeo-36-31-2013

Zazoun RS, Kadri MA, Cherigui A, Briedj M (2012) Le séisme du 14 Mai 2010 de Beni-Ilmane (M'sila, Algerie), (Ms = 5.2), Analyse des traces de surface. Bulletin du service Géologique National 23(1):85–101